Mechanics of diseased red blood cells in human spleen and consequences for hereditary blood disorders

Li et al. 10.1073/pnas.1806501115

Supporting Information (SI)

Two-component RBC Model and Validation

Two-component RBC model. In the coarse-grained molecular dynamics (CGMD) RBC model, the major two components of the RBC membrane, namely the cytoskeleton and the lipid bilayer, are represented explicitly by coarse grained (CG) particles. As shown in Fig. 1, the cytoskeleton of the membrane consists of spectrin filaments connected at the actin junctional complexes, forming a hexagonal network. The actin junctional complexes, represented by blue particles, are connected to the lipid bilayer via glycophorin proteins (yellow particles). Spectrin is a protein tetramer formed by two identical heterodimers. Each heterodimer is comprised of an α-chain with 22 triple-helical segments and a β-chain with 17 triple-helical segments. Thus, each spectrin filament is simulated by 39 spectrin particles (green particles). These spectrin particles are connected with unbreakable springs $u_{spectrin} = k_{spectrin}(d-d_{eq})^2$, where $k_{spectrin}$ is the spring constant, d and d_{eq} are distance and equilibrium distance between two spectrin CG particles. The lipid bilayer and transmembrane proteins of the RBC membrane are represented by three types of CG particles (Fig. 1). The red CG particles denote aggregates of lipid molecules. The yellow particles signify glycophorin proteins which are connected to the blue particles by unbreakable springs. The black particles represent band-3 proteins that tether spectrin filaments to the lipid bilayer. These three types of CG particles interact via a pairwise potential similar to the Lennard-Jones potential. However, the employed interacting potential depends not only on the translational degrees of freedom of two interacting CG particles $\mathbf{d}_i$ and $\mathbf{d}_j$, but also on their rotational degrees of freedom $\mathbf{n}_i$ and $\mathbf{n}_j$. The potential is given by

$$u_{ij}(\mathbf{n}_i, \mathbf{n}_j, \mathbf{x}_{ij}) = u_R(d) + A(\alpha, a(\mathbf{n}_i, \mathbf{n}_j, \hat{\mathbf{x}}_{ij}))u_A(d), \quad [1]$$

$$u_R(d) = 1.4\epsilon\left(\frac{d_c - d}{d_c - d_{eq}}\right)^8, \quad [2]$$

$$u_A(d) = -2.8\epsilon\left(\frac{d_c - d}{d_c - d_{eq}}\right)^4, \quad [3]$$

$$A(\alpha, a(\mathbf{n}_i, \mathbf{n}_j, \hat{\mathbf{x}}_{ij})) = 1 + \alpha(a(\mathbf{n}_i, \mathbf{n}_j, \hat{\mathbf{x}}_{ij}) - 1), \quad [4]$$

$$\begin{aligned} a(\mathbf{n}_i, \mathbf{n}_j, \hat{\mathbf{x}}_{ij}) &= (\mathbf{n}_i \times \hat{\mathbf{x}}_{ij}) \cdot (\mathbf{n}_j \times \hat{\mathbf{x}}_{ij}) \\ &= \mathbf{n}_i \cdot \mathbf{n}_j - (\mathbf{n}_i \cdot \hat{\mathbf{x}}_{ij})(\mathbf{n}_j \cdot \hat{\mathbf{x}}_{ij}), \end{aligned} \quad [5]$$

where $\mathbf{x}_{ij} = \mathbf{d}_j - \mathbf{d}_i$, $d = |\mathbf{x}_{ij}|$ and $\hat{\mathbf{x}}_{ij} = \mathbf{x}_{ij}/d$. α is a parameter that tunes the bending stiffness of the RBC membrane. d_c is the cutoff distance of the potential and it is selected to be 2.6σ, where σ is the length unit of the system. ϵ is the energy unit. Actin and spectrin filaments interact with lipid bilayer and transmembrane proteins via a Lennard-Jones potential,

$$U_{LJ} = 4\epsilon\left[\left(\frac{\sigma}{d}\right)^{12} - \left(\frac{\sigma}{d}\right)^{6}\right] \quad d < d_{eq}. \quad [6]$$

Detailed information about this RBC model can be found in the authors' former work in Li et al. (1) and Tang et al. (2).

This RBC model can simulate an entire RBC by using ∼4 million CG particles using a single shared memory commodity workstation, but it is computationally expensive when simulating a long-time dynamic process such as a RBC passage through IES. In order to achieve higher computational efficiency, we apply a coarse model by using a fewer number of actin junctions in the RBC model. While the RBC membrane structure is preserved, we model 500 actin junctions in a single RBC (see Fig. 1), instead of a physiological value of ∼23867. Following the method applied in (3), the parameters in the coarse RBC model are recalibrated against experimental data to ensure the mechanical properties of the RBC are preserved. The coarse RBC model consists of 198965 CG particles and the length unit of the model is $\sigma = 35$ nm. The energy unit is $\epsilon = k_BT/0.22$, where k_B is the Boltzmann constant and the temperature of the system T is 300 K. The parameter that determines the bending stiffness of the RBC membrane, α, is selected to be 2.1. The translational motions of CG particles are governed by the Langevin equation

$$m_i\frac{d\mathbf{v}_i}{dt} = -\zeta\mathbf{v}_i + \mathbf{F}_i + \boldsymbol{\xi}_i, \quad [7]$$

where m_i and $\mathbf{v}_i$ are the mass and velocity of the CG particle i. $\mathbf{F}_i$ is deterministic force exerted on particle i and it results from the interacting potentials. ζ is the friction coefficient and it is selected to be $0.01m/\tau$, where τ is the time scale of the simulation and $m = 669$ kDa is the mass unit of the system. Selection of ζ will be further discussed in the following section. $\boldsymbol{\xi}_i$ is the random force, which has zero mean and variance of $2k_BT\zeta/\triangle t$. For numerical integration of the equations of motion, we use the velocity Verlet algorithm with a finite time step of $\triangle t = 0.01\tau$.

In this study, we simulate the healthy and diseased RBCs passage through IES using CGMD method where the timescale of the system cannot be calculated following the same strategy of molecular dynamics because CG particles represent a lump of atoms or molecules and thus are not real atoms. The correspondence between the simulation time and the physical time can be established via comparison with a referenced physical process. In our simulation, when driven by a pressure gradient of 5 Pa μm^{-1}, it takes approximately 190000τ for a RBC with surface area of 140 μm^2 and volume of 90 μm^3 to traverse IES. If we correspond this simulation time to the median transition time of 0.23 s for RBC passage through IES measured from *in vivo* studies of rate model (4, 5), τ can be calculated to be 1.21×10^{-6} s.

The mechanical properties of mature RBCs mainly result from their cell membrane as they lack of nucleus and most organelles. The lipid bilayer of the RBC membrane behaves like 2D-fluid and thus the elasticity of RBCs arises primarily

from cytoskeleton. In the following sections, we will illustrate that the elastic properties and bending stiffness of the coarse RBC model are consistent with the previously reported experimental results by performing optical tweezer simulations and by measuring the thermal fluctuations of the RBC membrane.

Elastic properties of the RBC model. Optical tweezers have been successfully implemented to study the elasticity and deformability of RBCs (6, 7). A number of numerical simulations have mimicked this experimental setup by applying stretching forces on the opposite sides of RBCs to validate the RBC models and to probe the biomechanical behavior of diseased RBCs (8, 9). Following previous studies, we put the RBC model under stretch, analogous to the optical tweezer experiments, to examine the elasticity of the healthy and diseased RBCs. The total stretching force, F_s, is applied at the two ends of the RBCs in diametrically opposite directions, as shown in Fig. S1A. The stretching force is varied from 0 pN to 200 pN in increments of 20 pN. The stretch response of the RBC is measured by recording the axial (D_A) and transverse (D_T) diameters of the stretched RBC. Our simulations show that as the F_s increases, D_A of the RBC model increases whereas D_T decreases. Fig. S1B shows a RBC under a stretching force of 200 pN. As plotted in Fig. S2, the overall stretching response measured from the RBC model (blue curve) under various values of F_s is consistent with previous optical tweezer measurements of healthy RBCs (red curve) (7), which assumes a shear modulus of 5.3 pN/μm for the RBC model.

Bending stiffness of the RBC model. In this section, we validate the bending stiffness of the RBC model based on Brownian flicker analysis of membrane thermal fluctuations (10). We perform simulations following the protocol of a prior diffraction phase microscopy experiment (10), where the instantaneous heights of the cell membrane along the upper rim of a RBC were monitored to calculate the fluctuations of a RBC. In our simulation, the bottom of the RBC model is fixed, mimicking adhesion of the RBC to a solid substrate. The thermal fluctuation of the membrane is measured on the upper side of the RBC, through which the root-mean-square displacement (rmsd) of membrane fluctuations is calculated. Fig. S3 illustrates that the membrane fluctuation distribution of the RBC model overlaps with the measurements from the healthy RBCs in (10). The rmsd of the membrane fluctuations is computed to be about 90 nm. Based on the analytical expression derived in (11), the bending stiffness of the RBC, k_c, can be estimated by $k_c = Ak_BT/(8\pi^3 \text{rmsd}^2)$, where A is the surface area of a RBC. Following this expression, k_c of the RBC model is calculated to be 2.89×10^{-19} J, which falls within the range of 2×10^{-19} J to 7×10^{-19} J reported in prior experimental studies (12).

Cause of increased critical pressure gradient. The discrepancy between the critical pressure gradient of ~5 Pa μm^{-1} obtained in current work and the value of ~1 Pa μm^{-1} reported in previous studies is mainly attributed to the fact that the implemented CGMD RBC model is an implicit-solvent model. Implicit representation of solvent particles could underestimate the effect of the driven pressure. In addition, we cannot explicitly consider the effects of friction and hydrodynamic lubrication between the RBCs and the wall of IES with this implicit-solvent model. To examine the effects of

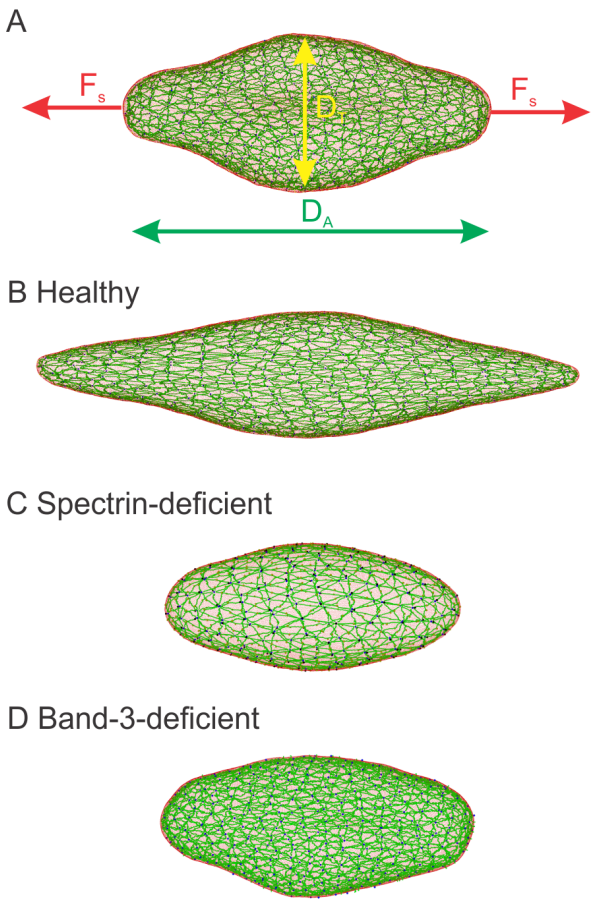

Fig. S1. Modeling the healthy and HS RBCs under stretch. (A) A stretching force, F_s, is applied at the two ends of a RBC in diametrically opposite directions. The axial (D_A) and transverse (D_T) diameters of the stretched RBC are recorded at a variety of F_s. (B) A healthy RBC under a stretching force of 200 pN. (C) A spectrin-deficient RBC with spectrin density of 40% under a stretching force of 200 pN. (D) A band-3-deficient RBC with vertical connectivity of 0% under a stretching force of 200 pN. In the above figures, the lipid particles (red particles) are plotted in a smaller size in order to more clearly visualize cytoskeleton (green particles).

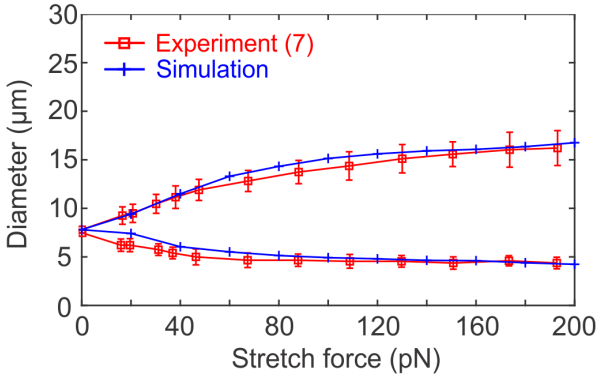

Fig. S2. The stretching response of a healthy RBC model under stretching forces ranging from 0 pN to 200 pN measured from our simulation and from optical tweezer experiments performed by Suresh et al. (7).

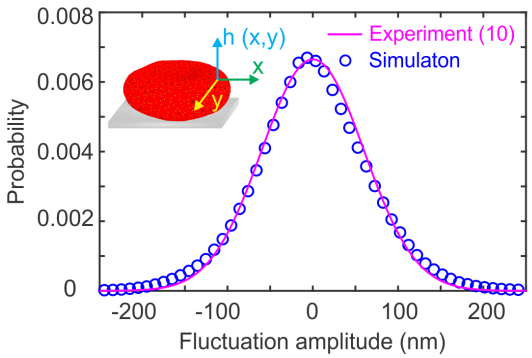

Fig. S3. Membrane fluctuation distributions measured at the upper rim of a healthy RBC measured from simulation (circles) and from experiment performed by Park et al. (10) (solid lines).

these simplifications, we perform DPD-based simulations, as reported in (13), and apply the pressure gradients on different components of blood: (*a*) RBC membrane only (an analogous simulation setup to our current study), and (*b*) both RBC membrane and solvent particles (the same simulation setup as in (13)). Indeed, we find that when driving the RBC through IES, the *equivalent* pressure gradient applied in case (*a*) is at least twice as much as that in case (*b*). Our implicit-solvent model did not consider the lubrication effect induced by the fluid flow around the RBC, which facilitates the RBC traversal process. Moreover, the interaction between the RBC and wall of IES is described by a hard core repulsive potential (Lennard-Jones potential) in our present model, whereas a soft-core repulsive potential was implemented in the DPD model. Implementation of a hard core repulsive potential also contributes to the increased critical pressure in the current model.

We also examine how the friction coefficient ζ in Eq.(7) affects the critical pressure that is able to drive RBCs through IES. First, we reduce the magnitude of ζ from 0.01 (used in current simulations) to 0.001 and we find that when ζ is reduced down to 0.004, the critical pressure gradient decreases from 5 to 3 Pa µm^{-1}. However, the temperature of the system is 5% lower than the target temperature, meaning that the thermostat cannot maintain the temperature of the system due to this small value of ζ. Next, we further reduce the value of ζ to 0.0001. We find that the system temperature can deviate from the target temperature by ∼10% whereas the critical pressure gradient remains at 3 Pa µm^{-1}. This result implies that reduction of ζ cannot decrease the critical pressure gradient while maintaining the temperature of the system when $\zeta \leq 0.01$. On the other hand, we also increase ζ from 0.01 to 0.1. Our simulation results show that when ζ is increased to 0.06 and 0.1, the critical pressure gradient is increased to 8 and 15 Pa µm^{-1}, respectively. These results show that the critical pressure gradient becomes sensitive to ζ when $\zeta \geq 0.06$.

It is noted that in spite of the discrepancy in the critical pressure gradient, we show that the critical ratio of S/V measured from our simulation, which determines the passage of RBCs through IES, is in agreement with the critical ratio of S/V obtained from the analytical model and DPD-based simulations in (13, 14). This finding suggests that application of a pressure gradient of 5 Pa µm^{-1} in the present model is equivalent to application of a pressure gradient of 1 Pa µm^{-1} in the DPD-based RBC model.

Analytical framework. Pivkin et.al (13, 14) developed a simplified axisymmetric model to elucidate the effects of geometric constraints on RBC–IES interactions. In their work, the slit cross-section in the y-z plane is assumed to be circular (Fig. S4) instead of rectangular, but with the same cross-sectional area such that

$$D_s = 2\sqrt{H_s W_s/\pi}. \quad [8]$$

Thus, the IES is approximated by the surface of a torus. As shown in Fig. S4, the traversing RBC at the critical condition is comprised of a central torus connected with two spheres. The surface area and volume of the RBC, therefore, can be computed by

$$A = 4\left(2\pi R^2 - \pi R h\right) + 2\pi L_s \theta \left(\frac{D_s}{2} + \frac{L_s}{2} - \frac{L_s \sin\theta}{2\theta}\right) \quad [9]$$

and

$$\begin{aligned} V =& 2\left[\frac{4}{3}\pi R^3 - \frac{1}{3}\pi h^2 (3R - h)\right] \\ &+ \frac{\pi L_s}{2}\left(R + \frac{L_s}{2}\right)\cos\theta(R\sin 2\theta - L_s\theta) \\ &+ \frac{\pi}{4}\left(L_s^3 \sin\theta - \frac{L_s^3 \sin^3\theta}{3}\right) \end{aligned} \quad [10]$$

respectively, where h is the height of spherical cap cut by the y-z plane at intersecting point p (Fig. S4) and

$$h = R - R\sqrt{1 - \frac{\left(\frac{D_s}{2} + \frac{L_s}{2}\right)^2}{\left(R + \frac{L_s}{2}\right)^2}} \quad [11]$$

and

$$\theta = \arccos\left[\left(\frac{D_s}{2} + \frac{L_s}{2}\right) / \left(R + \frac{L_s}{2}\right)\right] \quad [12]$$

is an angle of the torus part as shown in Fig. S4. After rewriting the Eq. (10) as $V = f(R)$ and defining its inverse function as $R = f^{-1}(V)$, Eq. (11) and Eq. (12) can be expressed as $h = h(R) = h(f^{-1}(V)) = g_1(V)$ and $\theta = \theta(R) = \theta(f^{-1}(V)) = g_2(V)$. Based on the axisymmetric theory, the minimum surface area (A), below which the RBCs with fixed volume (V) are retained by the slit, is given by

$$\begin{aligned} A =& 4\left\{2\pi\left[f^{-1}(V)\right]^2 - \pi f^{-1}(V) g_1(V)\right\} \\ &+ 2\pi L_s g_2(V)\left\{\frac{D_s}{2} + \frac{L_s}{2} - \frac{L_s \sin\left[g_2(V)\right]}{2g_2(V)}\right\}. \end{aligned} \quad [13]$$

where D_s is the radius of the slit opening and L_s is the thickness of the sinus wall.

Deformability index of healthy and diseased RBCs. To quantify the deformability of the healthy RBC and HS RBCs after passage through IES, we subject these RBCs under stretch to compute their deformability index based on the deformations of RBCs. The deformability index is defined as $DI = (D_A - D_T)/(D_A + D_T)$, where D_A and D_T are the axial and transverse diameters of the stretched RBCs, as shown in Fig. S1A. The stretch force F_s is selected to be 200 pN such that DI of the healthy RBC model is calculated to be 0.596,

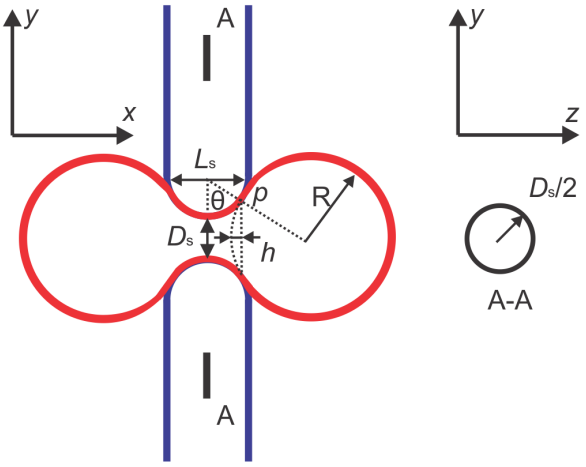

Fig. S4. Schematic of the slit geometry considered in the analytical model. The traversing RBC is signified by the red line. The surface of the RBC is tangential to the surfaces of the endothelial cells at point p. The black line circle on the right represents the cross-section A-A. The rectangular slit is approximated by the circular slit with the same cross-sectional area. Adapted from figure 2 in (13).

consistent with the DI of ∼0.61 measured by ektacytometry for healthy RBCs at a fixed osmolality of 300 mOsmol/kg (15). The average values of surface area loss reported in Fig. 4A are used to reconstruct the HS RBCs with various vertical connectivities and spectrin densities for DI measurements. Figs. S1C and D illustrate the deformations of a spectrin-deficient RBC with spectrin density of 40%, and a band-3-deficient RBC with zero vertical connectivity under stretching forces of 200 pN. Due to the decreased S/V ratio, the deformations of these two RBCs are suppressed, compared to the healthy RBC plotted in Fig. S1B. The DI of RBCs at different levels of intensity of molecular defects in HS is summarized in Fig. 4B.

Vesiculation process of band-3 deficient and spectrin-deficient HS RBCs. In case of band-3 deficient RBCs, although the vertical cohesion between lipid bilayer and cytoskeleton is impaired, the cytoskeleton is intact and the spectrin content is normal. Once a bud is initiated due to the localized dissociation between lipid bilayer and cytoskeleton (Fig. S5A), the lipids from neighboring membrane compartments flow to the localized dissociation area, which is evidenced by a growing tubular bud on the traversing band-3-deficient RBC (Fig. S5B and C). These observations are consistent with the mechanism proposed by Gov et.al (16). Subsequently, the necks of the buds become narrower and the vesicles are pinched off from the membrane (Fig. S5D–F). In case of spectrin-deficient RBCs, the number of actin junction complexes is reduced and the spectrin content is depleted. As illustrated in Fig. S6, multiple buds are formed from the spectrin-depleted area and subsequently separate from the RBC. These observations imply that the lipids in the spectrin-depleted area can bud off and form vesicles without pronounced lipid flow from neighboring compartments, consistent with the hypothesis raised by Elber et.al (17). Therefore, the mechanisms of RBC vesiculation are likely to depend on the type of protein deficiencies in HS.

SI Movies. Movie S1 A healthy RBC passing through IES under a pressure gradient of 20 Pa μm^{-1}. Only one half of the RBC is plotted for clarity.

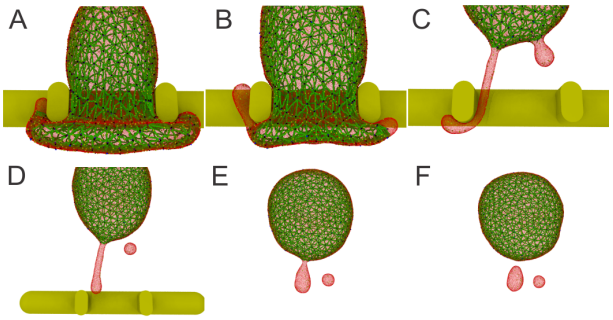

Fig. S5. Six sequential snapshots of the vesiculation process of an HS RBC with a vertical connectivity of 60% passage through IES under a pressure gradient of 10 Pa μm^{-1}.

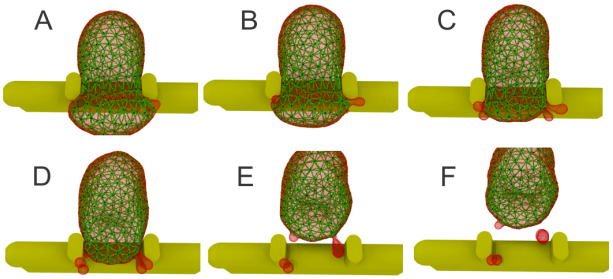

Fig. S6. Six sequential snapshots of the vesiculation process of an HS RBC with 60% spectrin content of normal RBCs passage through IES under a pressure gradient of 10 Pa μm^{-1}.

Movie S2 An HS RBC (top view) with a vertical connectivity of 60% passing through IES under a pressure gradient of 10 Pa μm^{-1}. The lipid CG particles (red particles) are plotted at a smaller size to visualize the underneath cytoskeleton (green particles).

Movie S3 An HE RBC (top view) with a horizontal connectivity of 50% passing through IES under a pressure gradient of 10 Pa μm^{-1}.

Movie S4 An HE RBC (top view) with a horizontal connectivity of 20% passing through IES under a pressure gradient of 10 Pa μm^{-1}.

References

1. Li H, Lykotrafitis G (2014) Erythrocyte membrane model with explicit description of the lipid bilayer and the spectrin network. *Biophysical Journal* 107(3):642–653.
2. Tang YH, et al. (2017) OpenRBC: A fast simulator of red blood cells at protein resolution. *Biophysical Journal* 112(10):2030–2037.
3. Pivkin IV, Karniadakis GE (2008) Accurate coarse-grained modeling of red blood cells. *Physical Review Letters* 101(11):118105.
4. Groom A, Schmidt E, MacDonald I (1991) Microcirculatory pathways and blood flow in spleen: new insights from washout kinetics, corrosion casts, and quantitative intravital videomicroscopy. *Scanning Microscopy* 5(1):159–73.
5. MacDonald I, Ragan D, Schmidt E, Groom A (1987) Kinetics of red blood cell passage through interendothelial slits into venous sinuses in rat spleen, analyzed by in vivo microscopy. *Microvascular Research* 33(1):118–134.
6. Dao M, Lim CT, Suresh S (2003) Mechanics of the human red blood cell deformed by optical tweezers. *Journal of the Mechanics and Physics of Solids* 51(11):2259–2280.
7. Suresh S, et al. (2005) Connections between single-cell biomechanics and human disease states: gastrointestinal cancer and malaria. *Acta Biomaterialia* 23:3–15.
8. Peng Z, et al. (2013) Lipid bilayer and cytoskeletal interactions in a red blood cell. *Proceedings of the National Academy of Sciences* 110(33):13356–13361.
9. Chang HY, Li X, Li H, Karniadakis GE (2016) MD/DPD multiscale framework for predicting morphology and stresses of red blood cells in health and disease. *PLOS Computational Biology* 12(10):e1005173.
10. Park Y, et al. (2008) Refractive index maps and membrane dynamics of human red blood cells parasitized by plasmodium falciparum. *Proc. Natl. Acad. Sci. U.S.A* 105(37):13730–13735.
11. Helfrich W, Servuss RM (1984) Undulations, steric interaction and cohesion of fluid membranes. *Il Nuovo Cimento D* 3(1):137–151.
12. Strey H, Peterson M, Sackmann E (1995) Measurement of erythrocyte membrane elasticity by flicker eigenmode decomposition. *Biophysical Journal* 69(2):478–488.

13. Pivkin IV, et al. (2016) Biomechanics of red blood cells in human spleen and consequences for physiology and disease. *Proceedings of the National Academy of Sciences* 113:7804–7809.
14. Pivkin IV, et al. (2017) Correction for Pivkin et al., Biomechanics of red blood cells in human spleen and consequences for physiology and disease. *Proceedings of the National Academy of Sciences* 114(22):E4521–E4521.
15. Walensky L (2003) *Disorders of the red blood cell membrane.* (Lippincott Williams & Wilkins), pp. 1709–1858.
16. Gov N, Cluitmans J, Sens P, Bosman G (2009) Cytoskeletal control of red blood cell shape: theory and practice of vesicle formation. *Advances in Planar Lipid Bilayers and Liposomes* 10:95–119.
17. Eber S, Lux SE (2004) Hereditary spherocytosis—defects in proteins that connect the membrane skeleton to the lipid bilayer. *Seminars in Hematology* 41(2):118–141.